VTT Technical Research Centre of Finland

Time-dependent neutronics model of nodal neutronics program Ants

Rintala, Antti; Lauranto, Unna

Published in:
Annals of Nuclear Energy

DOI:
10.1016/j.anucene.2023.109868

Published: 15/09/2023

Document Version
Publisher's final version

Annals of Nuclear Energy 190 (2023) 109868

Contents lists available at ScienceDirect

Annals of Nuclear Energy

journal homepage: www.elsevier.com/locate/anucene

Time-dependent neutronics model of nodal neutronics program Ants

Antti Rintala *, Unna Lauranto

VTT Technical Research Centre of Finland Ltd, P.O. Box 1000, FI-02044 VTT, Finland

ARTICLE INFO

Keywords:
Ants
Nodal neutronics
Time-dependent
FENM
AFEN

ABSTRACT

Ants is a nodal neutronics program developed at VTT since 2017. Ants solution method for the nodal diffusion equation is based on the function expansion nodal method (FENM) and analytic function expansion nodal (AFEN) method. Ants supports rectangular, hexagonal and triangular nodal geometries. The solution methodology of Ants extended to solve time-dependent problems is presented in this work. The performance of Ants is presented for all three geometry options in a series of established two- and three-dimensional numerical time-dependent benchmarks for both rectangular and hexagonal lattices. The Ants results agree with other published nodal program results, especially if the problem is not sensitive to control rod cusping effects or a fine enough axial mesh is used.

1. Introduction

Ants is a nodal neutronics program developed at VTT Technical Research Center of Finland Ltd (VTT) since 2017. Ants is a part of the Kraken computational framework for coupled core physics calculations (Leppänen et al., 2022). Previously Ants has been demonstrated together with the multi-physics driver program Cerberus to perform steady state and burnup calculations. The steady state methodology and performance in numerical benchmarks have been demonstrated for rectangular (Sahlberg and Rintala, 2018), hexagonal (Rintala and Sahlberg, 2019) and triangular (Hirvensalo et al., 2021) nodal geometries. The extension from nodal solutions to pin power reconstruction has been presented for rectangular (Valtavirta et al., 2022b) and hexagonal (Valtavirta et al., 2022a) geometries. Results of coupled fuel cycle simulations have been published in e.g. Valtavirta and Tuominen (2021) and Tuominen and Valtavirta (2023).

In order to expand the application area of Kraken to core-and plant level transient analyses, the FENM/AFEN-based nodal diffusion solution method of Ants has been extended to solve the time-dependent diffusion equation. The methodologies for all three supported nodal geometry options are presented in this work, including the three-dimensional triangular geometry, for which no AFEN or FENM based methods have been previously published to the best of the authors' knowledge. The solution method is based on decomposing the time-dependent diffusion equation solution to an analytic and a polynomial part (Kim and Cho, 2002). The analytic part is solved with the steady state solution methodology of Ants. A particular solution consisting of orthogonal polynomials is used in the full equation containing an inhomogeneous term. The final solution of the neutron flux is found as the sum of the analytic and polynomial solutions.

The purpose of this paper is to present the Ants solution method for the time-dependent nodal diffusion equation (Section 2), and to demonstrate its performance for all three supported nodal geometry options in various established numerical benchmarks (Section 3).

2. Ants time-dependent neutronics model

Multiple nodal methods for solving the diffusion equation have been developed in the past (Cho, 2005). The steady state model developed for Ants is based on the flux expansion nodal method (FENM) (Xia and Xie, 2006) and includes linear transverse gradient terms similar to some analytic function expansion nodal (AFEN) method variants (Woo et al., 2001). The multigroup problems with possible complex valued eigenvalues are solved with the method presented in Cho et al. (1997). The extensions of FENM and AFEN to solve time-dependent problems, on which the Ants time-dependent methodology is based on, have been presented in Xia et al. (2006) and Kim and Cho (2002).

2.1. Formulation of the time-dependent problem

The equations governing the time-dependent solution of the nodal diffusion method are the time-dependent diffusion equation for a homogeneous node for group g $(g = 1, \ldots, G)$

$$\frac{1}{v_g}\frac{\partial \phi_g(\mathbf{r},t)}{\partial t} = D_g(t)\nabla^2\phi_g(\mathbf{r},t) - \Sigma_{\mathrm{r},g}(t)\phi_g(\mathbf{r},t) + \sum_{g'\neq g}\Sigma_{g'\to g}(t)\phi_{g'}(\mathbf{r},t) + \chi_{\mathrm{d},g}\sum_{d=1}^{D}\lambda_d C_d(\mathbf{r},t) + (1-\beta)\frac{\chi_{\mathrm{p},g}}{k_{\mathrm{eff}}}\sum_{g'=1}^{G}\nu\Sigma_{\mathrm{f},g'}(t)\phi_{g'}(\mathbf{r},t) \quad (1)$$

* Corresponding author.
E-mail address: antti.rintala@vtt.fi (A. Rintala).

https://doi.org/10.1016/j.anucene.2023.109868
Received 7 November 2022; Received in revised form 6 March 2023; Accepted 12 April 2023
Available online 27 April 2023

and the precursor number density equation for a homogeneous node for delayed neutron precursor group d ($d = 1, \ldots, D$)

$$\frac{\partial C_d(\mathbf{r},t)}{\partial t} = \frac{\beta_d}{k_{\text{eff}}} \sum_{g=1}^{G} \nu\Sigma_{\text{f},g}(t)\phi_g(\mathbf{r},t) - \lambda_d C_d(\mathbf{r},t). \tag{2}$$

The notation in these equations is:

- v_g neutron speed of group g
- $\phi_g(\mathbf{r},t)$ neutron flux at $\mathbf{r}$ of group g
- $D_g(t)$ diffusion coefficient of group g
- $\Sigma_{\text{r},g}(t)$ removal group constant of group g
- $\Sigma_{g'\to g}(t)$ group-to-group transfer constant from group g' to group g
- $\chi_{\text{d},g}$ fraction of delayed neutrons born from precursor decay in group g
- λ_d delayed neutron precursor decay constant of delayed neutron precursor group d
- $C_d(\mathbf{r},t)$ delayed neutron precursor density at $\mathbf{r}$ of delayed neutron precursor group d
- β total delayed neutron fraction $\left(\beta = \sum_{d=1}^{D} \beta_d\right)$
- $\chi_{\text{p},g}$ fraction of prompt neutrons born from fission in group g
- k_{eff} steady state calculation effective multiplication factor
- $\nu\Sigma_{\text{f},g}(t)$ fission neutron production group constant of group g
- β_d delayed neutron fraction of delayed neutron precursor group d

The steady state k_{eff} is included in the equations to pronounce the fact that a time-dependent solution is initialized with a steady state solution to obtain an initial equilibrium at the beginning of a time-dependent calculation.

The time derivative of the neutron flux in Eq. (1) is discretized by using exponential transformation (Reed and Hansen, 1970) of the neutron flux $\phi_g(\mathbf{r},t)$ and using implicit Euler discretization for the transformed flux $\tilde{\phi}_g(\mathbf{r},t)$ (Kim and Cho, 2002). The exponential transformation is written as

$$\phi_g(\mathbf{r},t) = \mathrm{e}^{\omega_{n,g}(t-t_n)}\tilde{\phi}_g(\mathbf{r},t) \tag{3}$$

for a time-interval $t \in [t_n, t_{n+1}]$. The frequency $\omega_{n,g}$ is defined for group g as

$$\omega_{n,g} = \frac{1}{\Delta t_{n-1}} \ln \frac{\phi_g(t_n)}{\phi_g(t_{n-1})} \tag{4}$$

for a time step $\Delta t_{n-1} = t_n - t_{n-1}$ and the node-integrated neutron flux of group g $\phi_g(t_n) = \int_V \phi_g(\mathbf{r},t_n)\mathrm{d}V$, where V is the node volume. It is also possible to update the frequencies during the iteration of a time step with the newest group-wise fluxes of the current time step.

With the transformed flux, the time derivative of the flux can be expressed as

$$\frac{\partial \phi_g(\mathbf{r},t)}{\partial t} = \left(\omega_{n,g}\mathrm{e}^{\omega_{n,g}(t-t_n)}\right)\tilde{\phi}_g(\mathbf{r},t) + \left(\mathrm{e}^{\omega_{n,g}(t-t_n)}\right)\frac{\partial \tilde{\phi}_g(\mathbf{r},t)}{\partial t}. \tag{5}$$

Using the implicit Euler discretization for the time derivative of the transformed flux

$$\left.\frac{\partial \tilde{\phi}_g(\mathbf{r},t)}{\partial t}\right|_{t=t_{n+1}} = \frac{\tilde{\phi}_g(\mathbf{r},t_{n+1}) - \tilde{\phi}_g(\mathbf{r},t_n)}{\Delta t_n} \tag{6}$$

and the transformation of Eq. (3) in the opposite direction, the time derivative of the neutron flux (Eq. (5)) can be written as

$$\left.\frac{\partial \phi_g(\mathbf{r},t)}{\partial t}\right|_{t=t_{n+1}} = \left(\omega_{n,g} + \frac{1}{\Delta t_n}\right)\phi_g(\mathbf{r},t_{n+1}) - \frac{\mathrm{e}^{\omega_{n,g}\Delta t_n}}{\Delta t_n}\phi_g(\mathbf{r},t_n). \tag{7}$$

The precursor densities are solved from Eq. (2) using the exponential transform of Eq. (3), assuming that the terms $\nu\Sigma_{\text{f},g}(t)\tilde{\phi}_g(\mathbf{r},t)$ are linear between times t_n and t_{n+1}, and integrating the resulting equations analytically. The result is

$$C_d(\mathbf{r},t_{n+1}) = C_d(\mathbf{r},t_n)\mathrm{e}^{-\lambda_d\Delta t_n} + \frac{1}{k_{\text{eff}}}\sum_{g=1}^{G} F_{d,g}^{0,n}\nu\Sigma_{\text{f},g}(t_n)\phi_g(\mathbf{r},t_n) + \frac{1}{k_{\text{eff}}}\sum_{g=1}^{G} F_{d,g}^{1,n}\nu\Sigma_{\text{f},g}(t_{n+1})\phi_g(\mathbf{r},t_{n+1}), \tag{8}$$

where the terms $F_{d,g}^{0,n}$ and $F_{d,g}^{1,n}$ are

$$F_{d,g}^{0,n} = \frac{\beta_d}{\lambda_d + \omega_{n,g}}\left(\frac{\mathrm{e}^{\omega_{n,g}\Delta t_n} - \mathrm{e}^{-\lambda_d\Delta t_n}}{\Delta t_n(\lambda_d + \omega_{n,g})} - \mathrm{e}^{-\lambda_d\Delta t_n}\right) \tag{9}$$

and

$$F_{d,g}^{1,n} = \frac{\beta_d}{\lambda_d + \omega_{n,g}}\left(\mathrm{e}^{\omega_{n,g}\Delta t_n} - \frac{\mathrm{e}^{\omega_{n,g}\Delta t_n} - \mathrm{e}^{-\lambda_d\Delta t_n}}{\Delta t_n(\lambda_d + \omega_{n,g})}\right)\mathrm{e}^{-\omega_{n,g}\Delta t_n}. \tag{10}$$

This is equivalent to the result presented in Kim and Cho (2002), but with the result presented for the flux instead of the transformed flux.

Applying Eqs. (7) and (8) in Eq. (1), the discretized time-dependent neutron diffusion equation is obtained as

$$\begin{aligned} V_g^{1,n}\phi_g(\mathbf{r},t_{n+1}) - V_g^{0,n}\phi_g(\mathbf{r},t_n) - D_g(t_{n+1})\nabla^2\phi_g(\mathbf{r},t_{n+1}) + \Sigma_{\text{r},g}(t_{n+1})\phi_g(\mathbf{r},t_{n+1}) \\ = \sum_{g'\neq g}\Sigma_{g'\to g}(t_{n+1})\phi_{g'}(\mathbf{r},t_{n+1}) + (1-\beta)\frac{\chi_{\text{p},g}}{k_{\text{eff}}}\sum_{g'=1}^{G}\nu\Sigma_{\text{f},g'}(t_{n+1})\phi_{g'}(\mathbf{r},t_{n+1}) \\ + \chi_{\text{d},g}\sum_{d=1}^{D}\lambda_d\left(C_d(\mathbf{r},t_n)\mathrm{e}^{-\lambda_d\Delta t_n} + \frac{1}{k_{\text{eff}}}\sum_{g'=1}^{G}F_{d,g'}^{0,n}\nu\Sigma_{\text{f},g'}(t_n)\phi_{g'}(\mathbf{r},t_n)\right. \\ \left. + \frac{1}{k_{\text{eff}}}\sum_{g'=1}^{G}F_{d,g'}^{1,n}\nu\Sigma_{\text{f},g'}(t_{n+1})\phi_{g'}(\mathbf{r},t_{n+1})\right), \end{aligned} \tag{11}$$

where the terms $V_g^{0,n}$ and $V_g^{1,n}$ are

$$V_g^{0,n} = \frac{\mathrm{e}^{\omega_{n,g}\Delta t_n}}{v_g\Delta t_n} \tag{12}$$

and

$$V_g^{1,n} = \frac{1}{v_g}\left(\omega_{n,g} + \frac{1}{\Delta t_n}\right). \tag{13}$$

2.2. Solution of the time-dependent problem

Following the procedures of Kim and Cho (2002) and Xia et al. (2006), Eq. (11) is solved as a sum of an analytic and a polynomial parts. Gathering terms of Eq. (11), the equation can be written as

$$\begin{aligned} -D_g(t_{n+1})\nabla^2\phi_g(\mathbf{r},t_{n+1}) + \Sigma_{\text{r},g}(t_{n+1})\phi_g(\mathbf{r},t_{n+1}) - \sum_{g'\neq g}\Sigma_{g'\to g}(t_{n+1})\phi_{g'}(\mathbf{r},t_{n+1}) \\ - \frac{\chi_{\text{p},g}}{k_{\text{eff}}}\sum_{g'=1}^{G}\nu\Sigma_{\text{f},g'}(t_{n+1})\phi_{g'}(\mathbf{r},t_{n+1}) = S_g^{\text{eff}}(\mathbf{r},t_{n+1}), \end{aligned} \tag{14}$$

where the effective source term S_g^{eff} is

$$\begin{aligned} S_g^{\text{eff}}(\mathbf{r},t_{n+1}) = -V_g^{1,n}\phi_g(\mathbf{r},t_{n+1}) + V_g^{0,n}\phi_g(\mathbf{r},t_n) \\ - \beta\frac{\chi_{\text{p},g}}{k_{\text{eff}}}\sum_{g'=1}^{G}\nu\Sigma_{\text{f},g'}(t_{n+1})\phi_{g'}(\mathbf{r},t_{n+1}) \\ + \chi_{\text{d},g}\sum_{d=1}^{D}\lambda_d\left(C_d(\mathbf{r},t_n)\mathrm{e}^{-\lambda_d\Delta t_n} + \frac{1}{k_{\text{eff}}}\sum_{g'=1}^{G}F_{d,g'}^{0,n}\nu\Sigma_{\text{f},g'}(t_n)\phi_{g'}(\mathbf{r},t_n)\right. \\ \left. + \frac{1}{k_{\text{eff}}}\sum_{g'=1}^{G}F_{d,g'}^{1,n}\nu\Sigma_{\text{f},g'}(t_{n+1})\phi_{g'}(\mathbf{r},t_{n+1})\right). \end{aligned} \tag{15}$$

Writing the previous equation in a matrix form results into

$$-\nabla^2\boldsymbol{\phi}(\mathbf{r},t_{n+1}) + \mathbf{L}(t_{n+1})\boldsymbol{\phi}(\mathbf{r},t_{n+1}) = \mathbf{D}^{-1}(t_{n+1})\mathbf{S}^{\text{eff}}(\mathbf{r},t_{n+1}), \tag{16}$$

where $\boldsymbol{\phi}(\mathbf{r},t_{n+1})$ is a vector of group-wise neutron fluxes, $\mathbf{D}$ is a diagonal matrix of group-wise diffusion coefficients, $\mathbf{S}^{\text{eff}}$ is a vector of

group-wise effective source terms of Eq. (15) and

$$\mathbf{L}(t_{n+1}) = \mathbf{D}^{-1}(t_{n+1})\left(\mathbf{A}(t_{n+1}) - \frac{\chi_\mathrm{p}}{k_\mathrm{eff}}\mathbf{f}^\top(t_{n+1})\right), \tag{17}$$

where $\mathbf{A}(t)$ is a matrix with elements $A_{gg'}(t) = \delta_{gg'}\Sigma_{\mathrm{r},g}(t) - (1-\delta_{gg'})\Sigma_{g'\to g}(t)$, χ_p is a vector of prompt neutron fission yields and $\mathbf{f}(t_{n+1})$ is a vector of group-wise fission neutron production constants.

The homogeneous part of Eq. (16) is equivalent with the steady state equation solved in Ants (Sahlberg and Rintala, 2018; Rintala and Sahlberg, 2019; Hirvensalo et al., 2021), and the analytic part of the solution $\boldsymbol{\phi}_\mathrm{a}(\mathbf{r}, t_{n+1})$ is chosen to fulfill this equation, i.e.

$$-\nabla^2\boldsymbol{\phi}_\mathrm{a}(\mathbf{r}, t_{n+1}) + \mathbf{L}(t_{n+1})\boldsymbol{\phi}_\mathrm{a}(\mathbf{r}, t_{n+1}) = \mathbf{0}. \tag{18}$$

With this selection, the inhomogeneous term $\mathbf{S}^\mathrm{eff}(\mathbf{r}, t_{n+1})$ contains also terms depending on the current time step, and not only values depending on the previous time step, and the approximate polynomial part $\boldsymbol{\phi}_\mathrm{p}(\mathbf{r}, t_{n+1})$ necessary to fully solve Eq. (14) is used also in the solution of those terms. This selection is present also in the formulation of Kim and Cho (2002), and is explained with more detail in Joo et al. (1998). The selection preserves the initial steady state solution in case of a null transient.

The analytic solution method of Ants for Eq. (18) is presented in Sahlberg and Rintala (2018) for rectangular geometry, Rintala and Sahlberg (2019) for hexagonal geometry and Hirvensalo et al. (2021) for triangular geometry. In short, an eigenvalue decomposition

$$\mathbf{L} = \mathbf{U}\boldsymbol{\Lambda}\mathbf{U}^{-1} \tag{19}$$

is performed for matrix $\mathbf{L}$, and a flux transformation

$$\boldsymbol{\psi}(\mathbf{r}) = \mathbf{U}^{-1}\boldsymbol{\phi}(\mathbf{r}) \tag{20}$$

is applied to obtain G decoupled equations

$$-\nabla^2\psi_m(\mathbf{r}) + \lambda_m\psi_m(\mathbf{r}) = 0, \tag{21}$$

where ψ_m is the mode flux of mode m, and λ_m is the mth diagonal value of $\boldsymbol{\Lambda}$. Analytic solutions for ψ_m in different nodal geometries can be found. The solutions are weighted sums of L basis functions ψ_m^l which are either sine and cosine functions or hyperbolic sine and cosine functions depending on the sign of λ_m so that the complete solutions are

$$\psi_m = \sum_{l=1}^{L} c_m^l \psi_m^l. \tag{22}$$

Using the transformation of Eq. (20) in the opposite direction, the solutions for the flux can be presented as a sum of the mode flux solutions. In case of complex conjugate pair eigenvalues λ_m and λ_{m+1}, a slightly different transformation is used to obtain a loosely coupled equation pair. The analytic basis functions for these modes are different products of sine, cosine, hyperbolic sine and hyperbolic cosine functions, producing real-valued analytic solutions also for these modes with complex eigenvalues.

The full solution of Eq. (16) is obtained in a weighted integral sense. The polynomial part of the flux is expanded as a polynomial of order I such that

$$\phi_{\mathrm{p},g}(\mathbf{r}, t_{n+1}) = \sum_{i=1}^{I} c_{i,g}^{\mathrm{p},n+1} w_i(\mathbf{r}), \tag{23}$$

where $c_{i,g}^{\mathrm{p},n+1}$ is the polynomial expansion coefficient at time t_{n+1} for basis function i and group g. The basis functions $w_i(\mathbf{r})$ are selected to be orthonormal in a volume-integral sense for a node as

$$\int_V w_i(\mathbf{r})w_j(\mathbf{r})\mathrm{d}V = \delta_{ij}. \tag{24}$$

The polynomial basis functions utilized in Ants for the different nodal geometries are presented in Table 1. The normalization coefficients of the functions are uniquely determined by the orthonormality requirement.

Table 1
The polynomial basis functions $w_i(\mathbf{r})$ for different nodal geometries. Here x_h and y_h are the rectangular node widths in x and y direction, z_h is the node height, h is the hexagonal node flat-to-flat width, a is the side length of the equilateral triangle of the triangular node, and N_i are normalization coefficients. The hexagonal geometry basis functions originate from Xia et al. (2006), whereas the rectangular geometry basis functions are based on Legendre polynomials up to the second order (Kim and Cho, 2002).

i	Rectangular	Hexagonal	Triangular
1	$1/N_1$	$1/N_1$	$1/N_1$
2	x/N_2	x/N_2	x/N_2
3	y/N_3	y/N_3	y/N_3
4	z/N_4	z/N_4	z/N_4
5	$\left(\frac{3}{2}x^2 - \frac{1}{2}x_h^2\right)/N_5$	$\left(x^2 + y^2 - \frac{5}{9}h^2\right)/N_5$	$\left(x^2 + y^2 - \frac{1}{12}a^2\right)/N_5$
6	$\left(\frac{3}{2}y^2 - \frac{1}{2}y_h^2\right)/N_6$	$\left(x^2 - y^2\right)/N_6$	$\left(\frac{3}{2}z^2 - \frac{1}{2}z_h^2\right)/N_6$
7	$\left(\frac{3}{2}z^2 - \frac{1}{2}z_h^2\right)/N_7$	$2xy/N_7$	
8	xy/N_8	$\left(\frac{3}{2}z^2 - \frac{1}{2}z_h^2\right)/N_8$	
9	xz/N_9		
10	yz/N_{10}		

Substituting the neutron flux vector

$$\boldsymbol{\phi} = \boldsymbol{\phi}_\mathrm{a} + \boldsymbol{\phi}_\mathrm{p} \tag{25}$$

and Eq. (18) in Eq. (16), the result is

$$-\nabla^2\boldsymbol{\phi}_\mathrm{p}(\mathbf{r}, t_{n+1}) + \mathbf{L}(t_{n+1})\boldsymbol{\phi}_\mathrm{p}(\mathbf{r}, t_{n+1}) = \mathbf{D}^{-1}(t_{n+1})\mathbf{S}^\mathrm{eff}(\mathbf{r}, t_{n+1}). \tag{26}$$

Using Eq. (23), multiplying the resulting equation with a basis function $w_j(\mathbf{r})$ and integrating the result over the node volume, and denoting

$$s_{i,g}^{\mathrm{p},n+1} = \int_V w_i(\mathbf{r})S_g^\mathrm{eff}(\mathbf{r}, t_{n+1})\mathrm{d}V, \tag{27}$$

the final equation for solving the polynomial expansion coefficients is obtained as

$$-\int_V w_j(\mathbf{r})\sum_{i=1}^{I}\mathbf{c}_{i,g}^{\mathrm{p},n+1}\nabla^2 w_i(\mathbf{r})\mathrm{d}V + \mathbf{L}\mathbf{c}_{j,g}^{\mathrm{p},n+1} = \mathbf{D}^{-1}(t_{n+1})\mathbf{s}_{j,g}^{\mathrm{p},n+1}. \tag{28}$$

The first sum term in the previous equation is non-zero only for $j = 1$, and $i \in \{5, 6, 7\}$ in rectangular geometry, $i \in \{5, 8\}$ in hexagonal geometry and $i \in \{5, 6\}$ in triangular geometry. Therefore, the coefficient vectors $\mathbf{c}_{j,g}^{\mathrm{p},n+1}$ can first be solved for $j > 1$, and together with the obtained solutions for $j = 1$.

Denoting

$$c_{i,g}^{\phi,n+1} = \int_V w_i(\mathbf{r})\phi_g(\mathbf{r}, t_{n+1})\mathrm{d}V = \int_V w_i(\mathbf{r})\phi_{\mathrm{a},g}(\mathbf{r}, t_{n+1})\mathrm{d}V + \int_V w_i(\mathbf{r})\phi_{\mathrm{p},g}(\mathbf{r}, t_{n+1})\mathrm{d}V = c_{i,g}^{\mathrm{a},n+1} + c_{i,g}^{\mathrm{p},n+1} \tag{29}$$

and

$$c_{i,d}^{\mathrm{C},n+1} = \int_V w_i(\mathbf{r})C_d(\mathbf{r}, t_{n+1})\mathrm{d}V, \tag{30}$$

the source expansion coefficients of Eq. (27) can be calculated analytically as

$$\begin{aligned} s_{i,g}^{\mathrm{p},n+1} = {} & -V_g^{1,n}c_{i,g}^{\phi,n+1} + V_g^{0,n}c_{i,g}^{\phi,n} - \beta\frac{\chi_{\mathrm{p},g}}{k_\mathrm{eff}}\sum_{g'=1}^{G}\nu\Sigma_{\mathrm{f},g'}(t_{n+1})c_{i,g}^{\phi,n+1} \\ & + \chi_{\mathrm{d},g}\sum_{d=1}^{D}\lambda_d\left(c_{i,d}^{\mathrm{C},n}\mathrm{e}^{-\lambda_d\Delta t_n} + \frac{1}{k_\mathrm{eff}}\sum_{g'=1}^{G}F_{d,g'}^{0,n}\nu\Sigma_{\mathrm{f},g'}(t_n)c_{i,g}^{\phi,n}\right. \\ & \left. + \frac{1}{k_\mathrm{eff}}\sum_{g'=1}^{G}F_{d,g'}^{1,n}\nu\Sigma_{\mathrm{f},g'}(t_{n+1})c_{i,g}^{\phi,n+1}\right). \end{aligned} \tag{31}$$

The necessary flux expansion coefficients of Eq. (29) are analytically calculable, and the precursor expansion coefficients can be calculated

using them with Eqs. (8) and (30) to obtain

$$c_{i,d}^{\mathrm{C},n+1} = c_{i,d}^{\mathrm{C},n} \mathrm{e}^{-\lambda_d \Delta t_n} + \frac{1}{k_{\mathrm{eff}}} \sum_{g=1}^{G} F_{d,g}^{0,n} \nu \Sigma_{\mathrm{f},g}(t_n) c_{i,g}^{\phi,n} + \frac{1}{k_{\mathrm{eff}}} \sum_{g=1}^{G} F_{d,g}^{1,n} \nu \Sigma_{\mathrm{f},g}(t_{n+1}) c_{i,g}^{\phi,n+1}. \quad (32)$$

Therefore, it is not necessary to track the actual flux, fission source or precursor density distributions of the previous time step to obtain a flux solution of the current time step. Only the weighted integrals of the said quantities are needed.

The polynomial flux expansion coefficients can be solved uniquely from Eq. (28) with known expansion coefficients $c_{i,g}^{\phi,n+1}$. The analytic basis function expansion coefficients c_m^l (Eq. (22)) are solved using nodal boundary conditions as in Xia et al. (2006). The incoming and outgoing partial currents at a node surface k for group g can be written as

$$J_{g,k}^{\pm} = \frac{1}{4}\phi_{g,k} \mp \frac{1}{2} D_g \nabla \phi_{g,k} = \frac{1}{4}\phi_{\mathrm{a},g,k} \mp \frac{1}{2} D_g \nabla \phi_{\mathrm{a},g,k} + \frac{1}{4}\phi_{\mathrm{p},g,k} \mp \frac{1}{2} D_g \nabla \phi_{\mathrm{p},g,k}. \quad (33)$$

The partial currents of the form Eq. (33) weighted with unity or sign functions are used as boundary conditions in Ants. The numbers of boundary conditions are 18, 20 and 14 for rectangular, hexagonal and triangular nodal geometries, respectively. The time-dependent solution uses the same weighting functions as the steady state model described in Sahlberg and Rintala (2018), Rintala and Sahlberg (2019) and Hirvensalo et al. (2021) for the different geometries.

The result of analytic evaluation of the boundary conditions of Eq. (33) using Eqs. (20), (22), (23) and (25) can be collected into two matrix equations as

$$\mathbf{j}^{+}(t_{n+1}) = \mathbf{Q}_{\mathrm{a}}^{+,n+1} \mathbf{c}_{\mathrm{a}}^{n+1} + \mathbf{Q}_{\mathrm{p}}^{+,n+1} \mathbf{c}_{\mathrm{p}}^{n+1} \quad (34)$$

and

$$\mathbf{j}^{-}(t_{n+1}) = \mathbf{Q}_{\mathrm{a}}^{-,n+1} \mathbf{c}_{\mathrm{a}}^{n+1} + \mathbf{Q}_{\mathrm{p}}^{-,n+1} \mathbf{c}_{\mathrm{p}}^{n+1}. \quad (35)$$

Here $\mathbf{c}_{\mathrm{a}}^{n+1}$ is a vector of length $G \times L$ containing the coefficients c_m^l of Eq. (22), and $\mathbf{c}_{\mathrm{p}}^{n+1}$ is a vector of length $G \times I$ containing the coefficients $c_{i,g}^{\mathrm{p},n+1}$ of Eq. (23). The inner iteration of calculating outgoing partial current moments from incoming partial current moments can be solved from Eqs. (34) and (35) as

$$\mathbf{j}^{+}(t_{n+1}) = \mathbf{Q}_{\mathrm{a}}^{+,n+1} (\mathbf{Q}_{\mathrm{a}}^{-,n+1})^{-1} \mathbf{j}^{-}(t_{n+1}) + \left(\mathbf{Q}_{\mathrm{p}}^{+,n+1} - \mathbf{Q}_{\mathrm{a}}^{+,n+1} (\mathbf{Q}_{\mathrm{a}}^{-,n+1})^{-1} \mathbf{Q}_{\mathrm{p}}^{-,n+1}\right) \mathbf{c}_{\mathrm{p}}^{n+1}. \quad (36)$$

The coefficient vector $\mathbf{c}_{\mathrm{a}}^{n+1}$ can be solved from Eq. (35) as

$$\mathbf{c}_{\mathrm{a}}^{n+1} = \left(\mathbf{Q}_{\mathrm{a}}^{-,n+1}\right)^{-1} \left(\mathbf{j}^{-}(t_{n+1}) - \mathbf{Q}_{\mathrm{p}}^{-,n+1} \mathbf{c}_{\mathrm{p}}^{n+1}\right). \quad (37)$$

2.3. Coarse group rebalance

The convergence of outer iterations is accelerated using coarse group rebalance (CGR) method (Kim and Cho, 2002). With integration of Eq. (11) over the node volume V and summing over all groups, after reordering the equation can be written as

$$\sum_{g=1}^{G} V_g^{1,n} \phi_g(t_{n+1}) + \sum_{k=1}^{K} \sum_{g=1}^{G} (J_{k,g}^{+}(t_{n+1}) - J_{k,g}^{-}(t_{n+1})) + \sum_{g=1}^{G} \Sigma_{\mathrm{a},g}(t_{n+1}) \phi_g(t_{n+1}) - (1-\beta) \frac{1}{k_{\mathrm{eff}}} \sum_{g=1}^{G} \nu \Sigma_{\mathrm{f},g}(t_{n+1}) \phi_g(t_{n+1}) - \sum_{d=1}^{D} \lambda_d \frac{1}{k_{\mathrm{eff}}} \sum_{g=1}^{G} F_{d,g}^{1,n} \nu \Sigma_{\mathrm{f},g}(t_{n+1}) \phi_g(t_{n+1}) = \sum_{g=1}^{G} V_g^{0,n} \phi_g(t_n) + \sum_{d=1}^{D} \lambda_d \left(C_d(t_n) \mathrm{e}^{-\lambda_d \Delta t_n} + \frac{1}{k_{\mathrm{eff}}} \sum_{g=1}^{G} F_{d,g}^{0,n} \nu \Sigma_{\mathrm{f},g}(t_n) \phi_g(t_n) \right), \quad (38)$$

where all terms on the left hand side of the equation are dependent on the solution of the current time step, and terms on the right hand side act as a fixed source. Here ϕ_g is the node-integrated flux, $J_{k,g}^{+}$ and $J_{k,g}^{-}$ are the node face k integrated outgoing and incoming partial currents, respectively, and $\Sigma_{\mathrm{a},g}$ is the absorption group constant. Using the neighbor node outgoing partial current as the incoming partial current for the current node, and assuming a single rebalance coefficient f for the node-integrated neutron flux and the outgoing partial currents as

$$\phi_g(t_{n+1}) = f \tilde{\phi}_g(t_{n+1}) \quad (39)$$

and

$$J_{k,g}^{+}(t_{n+1}) = f \tilde{J}_{k,g}^{+}(t_{n+1}), \quad (40)$$

where the values marked with $\tilde{\cdot}$ are the values before the rebalance. To perform the rebalance simultaneously for all nodes, the Eqs. (38), (39) and (40) can be collected to a matrix equation as

$$\mathbf{M}\mathbf{f} = \mathbf{s}, \quad (41)$$

where the terms on the left hand side of Eq. (38) are included in the matrix $\mathbf{M}$ and the terms on the right hand side are included in the vector $\mathbf{s}$. The solution vector $\mathbf{f}$ are then used to rebalance all the flux and outgoing partial current dependent values of the nodes.

2.4. Iteration scheme

A time-dependent Ants calculation is initialized with the steady state multiplication factor k_{eff} and the flux and precursor density expansion coefficients $c_{i,g}^{\phi,n}$ and $c_{i,g}^{\mathrm{C},n}$ of Eqs. (29) and (30) for the beginning of the first time step values. For the first outer iteration, the same coefficients are used as the end of time step values. Afterwards, for each time step the following iteration procedure is followed:

1. Frequencies are updated using Eq. (4)
2. The source expansion coefficients are constructed using Eq. (31)
3. The polynomial flux expansion coefficients are solved from Eq. (28)
4. The eigenvalue decompositions of Eq. (19) are performed
5. The matrixes $\mathbf{Q}_{\mathrm{a}}^{+,n+1}$, $\mathbf{Q}_{\mathrm{a}}^{-,n+1}$, $\mathbf{Q}_{\mathrm{p}}^{+,n+1}$ and $\mathbf{Q}_{\mathrm{p}}^{-,n+1}$ of Eqs. (34) and (35) are constructed
6. N inner iterations of Eq. (36) are performed with red-black or four-color iteration to update node partial current moments using neighbor node outgoing partial current moments as the incoming partial current moments of the current node
7. The coefficients of the analytic flux are solved using Eq. (37)
8. Volume-integrated fluxes are calculated using analytic expressions of Eqs. (20), (22), (23) and (25)
9. Coarse group rebalance of Eq. (41) is performed
10. The flux expansion coefficients are calculated with Eq. (29)
11. If fluxes, fission sources and total power are converged, the outer iterations are stopped, otherwise a new outer iteration is performed beginning from step 1 or 2, depending on whether the frequency values are updated during the iteration of the time step

After convergence is obtained, the precursor density expansion coefficients are calculated with Eqs. (29) and (30) to be used during the iteration of the next time step.

3. Benchmarks and results

Five different benchmarks with a total of seven different compared cases are solved with the Ants time-dependent neutronics model. For

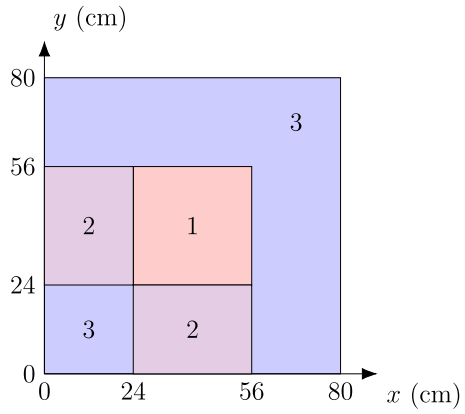

Fig. 1. TWIGL benchmark quarter core radial geometry.

Table 2
Effective multiplication factors of the initial state of the TWIGL benchmark.

Code	Ants	QUANDRY	POLCA7	SPANDEX
Radial mesh (cm^2)	8 × 8	8 × 8	8 × 8	4 × 4
k_{eff}	0.91321	0.91321	0.91321	0.91321

rectangular geometry, the two-dimensional TWIGL benchmark and the three-dimensional LMW and LRA problems are solved, and for the hexagonal and triangular geometries, the three-dimensional AER-DYN-001 and AER-DYN-002 benchmarks are solved. The Ants results are calculated using convergence criterion of the steady state multiplication factor difference between successive outer iterations being less than 10^{-9} and the relative change of node-wise fission source between successive outer iterations being less than 10^{-6}. In the LRA and AER-DYN-002 benchmarks the fuel temperature increase due to adiabatic heating is solved using implicit Euler discretization. Additionally, the Ants calculation times are presented in two example benchmarks and the effect of the temporal mesh on the solution accuracy is studied in one example benchmark at the end of this section.

3.1. TWIGL benchmark

The TWIGL benchmark is a two-dimensional kinetics problem with no modeled feedbacks (Hageman and Yasinsky, 1969). The geometry of the highly simplified model with a quarter core symmetry is shown in Fig. 1. Two energy groups and one delayed neutron precursor group are used in the problem. Two transient scenarios are included in the benchmark, where the absorption group constant of the assemblies indicated by "1" in the figure are either perturbed in a step-wise manner or with a linear ramp. The transients are followed for 0.5 s.

The benchmark results for Ants and a selection of other nodal programs are presented for the initial steady state effective multiplication factors k_{eff} in Table 2 and for the time-dependent powers in Tables 3 and 4 for the step and ramp perturbations, respectively. The data for programs other than Ants is collected from Smith (1979), Sutton and Aviles (1996) and Kotchoubey (2015). The full Ants time-dependent power solutions are plotted in Fig. 2 with a comparison against QUANDRY results.

The k_{eff} values are identical between the different programs in the presented accuracy, even though the SPANDEX results are solved using a finer mesh. The time-dependent power solutions show very little variation between the different solutions.

3.2. LMW benchmark

The LMW benchmark problem (Langenbuch et al., 1977; Smith, 1979) consists of an operational transient in a simplified three-dimensional

Table 3
TWIGL benchmark step perturbation transient results.

Code	Ants	QUANDRY	POLCA-T	SPANDEX
Radial mesh (cm^2)	8 × 8	12/16 × 12/16	8 × 8	4 × 4
Time step (ms)	10	10	10	0.1
Time (s)	Relative power (–)			
0.0	1.000	1.000	1.000	1.000
0.1	2.060	2.064	2.061	2.062
0.2	2.078	2.076	2.080	2.079
0.3	2.096	2.095	2.097	2.096
0.4	2.113	2.112	2.114	2.114
0.5	2.131	2.130	2.132	2.131

Table 4
TWIGL benchmark ramp perturbation transient results.

Code	Ants	QUANDRY	POLCA-T	SPANDEX
Radial mesh (cm^2)	8 × 8	8 × 8	8 × 8	4 × 4
Time step (ms)	5	2.5	5	0.1
Time (s)	Relative power (–)			
0.0	1.000	1.000	1.000	1.000
0.1	1.309	1.307	1.308	1.309
0.2	1.961	1.957	1.961	1.960
0.3	2.075	2.074	2.076	2.075
0.4	2.093	2.092	2.093	2.092
0.5	2.110	2.109	2.111	2.110

Table 5
Effective multiplication factors of the initial state of the LMW benchmark.

Code	Ants	Ants	QUANDRY	POLCA7	SPANDEX
Radial mesh (cm^2)	20 × 20	20 × 20	20 × 20	20 × 20	5 × 5
Axial mesh (cm)	20	2	20	20	2.5
k_{eff}	0.99966	0.99966	0.99974	0.99970	0.99964

PWR core with quarter core symmetry. The transient includes moderate movement of two control rod groups. The quarter core radial and axial geometries are shown in Fig. 3. The problem is modeled with two energy groups and six delayed neutron precursor groups. The problem excludes all thermal hydraulic feedbacks.

The transient is initiated with the movement of the originally inserted control rods of group 1. The group is withdrawn at a constant speed of 3 cm/s until it reaches the top of the active core. The insertion of control rod group 2 starts at 7.5 s with the same speed of 3 cm/s. The group is stopped at 60 cm elevation from the bottom of the core. The transient is followed for 60 s.

The benchmark results for Ants and a selection of other nodal programs are presented for the initial steady state effective multiplication factors k_{eff} in Table 5 and for the time-dependent powers in Table 6. The time-dependent solutions are selected among those having a fixed time step length 250 ms. The data for programs other than Ants is collected from Smith (1979), Sutton and Aviles (1996), Kotchoubey (2015) and Bahadir (2022). The full Ants time-dependent power solutions are plotted in Fig. 4 with a comparison against QUANDRY and SIMULATE5-K results.

The k_{eff} values are within 10 pcm between the presented results. The Ants values are closest to the finer mesh results calculated with SPANDEX.

As noted by other authors, the slow movement of control rods result into multiple partially rodded nodes during the transient. A proper homogenization of such nodes correctly accounting for the different flux values inside the rodded and to unrodded parts is essential for obtaining realistic results. Otherwise the control rod cusping effect will be evident. Currently, Ants does not have a model for correcting the cusping effect, which is clearly seen in the results with a coarse axial mesh (20 cm node height). The results are rather similar to those presented in Kotchoubey (2015) and Bahadir (2022) when the axial

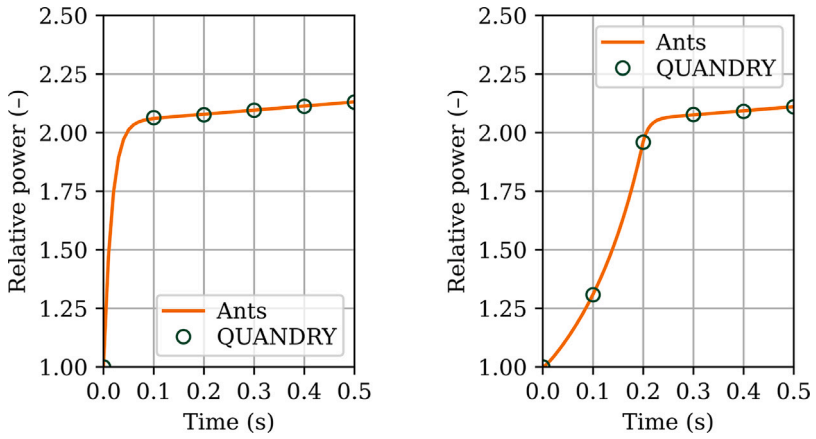

Fig. 2. Time-dependent powers in the TWIGL benchmark step perturbation (left) and ramp perturbation (right) transients. The solution parameters for the different programs are presented in Tables 3 and 4.

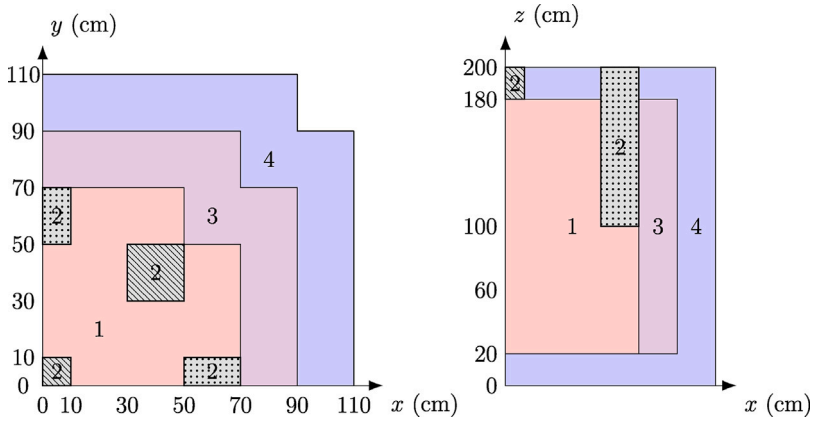

Fig. 3. LMW benchmark quarter core radial (left) and axial (right) geometries. The dotted assemblies indicate control rod group 1 and the assemblies with diagonal lines indicate control rod group 2.

Table 6
LMW benchmark transient results.

Code	Ants	Ants	QUANDRY	SIMULATE5-K
Radial mesh (cm^2)	20 × 20	20 × 20	20 × 20	20 × 20
Axial mesh (cm)	20	2	10	20
Time step (ms)	250	250	250	250
Time (s)	Power density (W/cm^3)			
0	150.0	150.0	150.0	150.0
5	168.1	169.0	169.1	169.0
10	197.4	201.0	202.0	201.8
20	249.1	256.5	262.2	257.7
30	198.5	205.6	210.8	206.6
40	118.1	121.3	123.0	121.9
50	73.7	75.4	75.7	75.7
60	56.6	57.9	57.9	57.9

homogenization methods are disabled. With the fine axial nodalization (2 cm node height) in Ants the effect is practically not seen.

QUANDRY uses an approximate method for calculating the partially rodded node group constants (Smith, 1979), whereas POLCA-T and SIMULATE5-K solve one-dimensional diffusion equations for each axial node stack to calculate the group constants and axial discontinuity factors (Kotchoubey, 2015; Bahadir, 2022). The Ants fine axial mesh results are closer to the SIMULATE5-K results than the QUANDRY results. The maximum relative difference between Ants coarse and fine axial meshes and the QUANDRY results are −5.9 % and −2.5 %, respectively, whereas SIMULATE5-K has a maximum relative difference of −2.0 %. The Ants maximum relative differences against SIMULATE5-K are −4.0 % and −0.5 % for the coarse and fine axial meshes, respectively.

Table 7
Effective multiplication factors of the initial state of the LRA benchmark.

Code	Ants	Ants	QUANDRY	POLCA7
Radial mesh (cm^2)	15 × 15	15 × 15	15 × 15	15 × 15
Axial mesh (cm)	15	1.5	15/30	15/30
k_{eff}	0.99641	0.99641	0.99644	0.99641

3.3. LRA benchmark

The LRA problem is a three-dimensional rod drop transient in a BWR core (Argonne Code Center, 1977; Smith, 1979; Sutton and Aviles, 1996). Two scenarios of the three-dimensional benchmark are calculated, a single-rod ejection event and a four-rod ejection event. The problem employs two energy groups and two delayed neutron precursor groups. The effects of fuel temperature change are modeled with adiabatic heatup and Doppler feedback mechanism.

The radial quarter core geometry and the axial configuration of the core are shown in Fig. 5. Zero flux boundary conditions are applied in the core periphery. Cruciform control rods are modeled within the four surrounding assemblies around the rod with material 3.

The simulation is performed in two separate transient scenarios: the single rod case, in which only the control rod shown in Fig. 5 is dropped

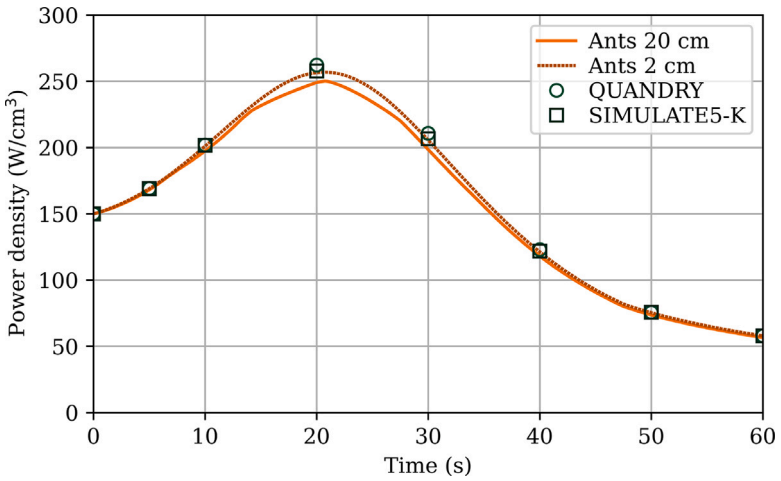

Fig. 4. Time-dependent powers in the LMW benchmark transient. The solution parameters for different programs are presented in Table 6.

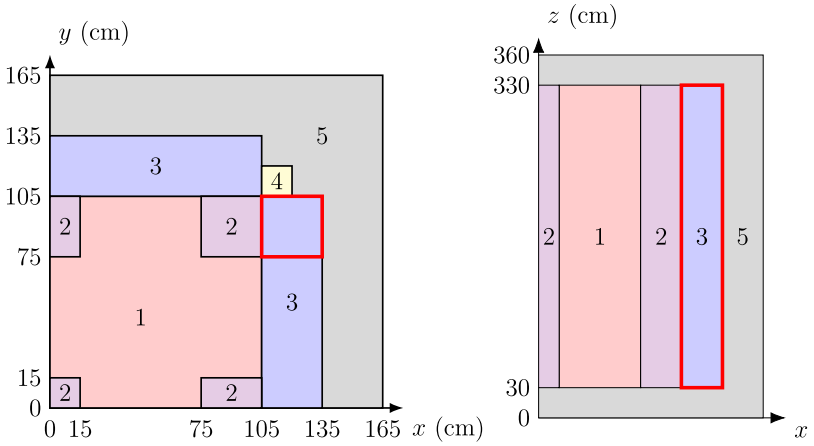

Fig. 5. LRA benchmark quarter core radial (left) and axial (right) geometries. The position of the dropped control rod is outlined with red.

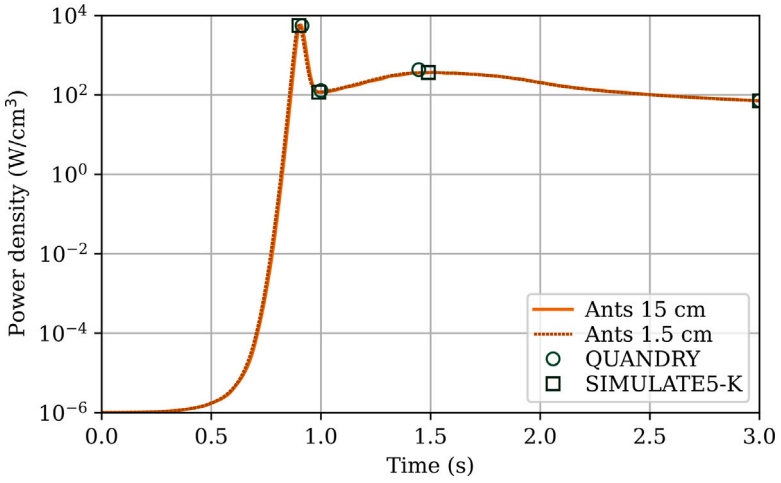

Fig. 6. Time-dependent powers in the LRA four rod benchmark transient. The solution parameters for different programs are presented in Table 8.

from the core at a constant speed of 150 cm/s, and the four rod case, in which all four rods symmetric to the rod indicated in the quarter core model are dropped at the same time with the same velocity of 150 cm/s. The transients are followed for 3 s.

The benchmark results for Ants and a selection of other nodal programs are presented for the initial steady state effective multiplication factors k_{eff} in Table 7 and for the time-dependent powers in Tables 8 and 9 for the four rod and single rod transients, respectively. The time steps used in Ants calculations are presented in Table 10. The data for programs other than Ants is collected from Smith (1979), Brega et al. (1981), Kotchoubey (2015) and Bahadir (2022). The full Ants time-dependent power solutions are plotted in Figs. 6 and 7 with comparisons against QUANDRY and SIMULATE5-K results.

The k_{eff} values are almost equal between the presented results, with the QUANDRY having a 3 pcm difference to the other results.

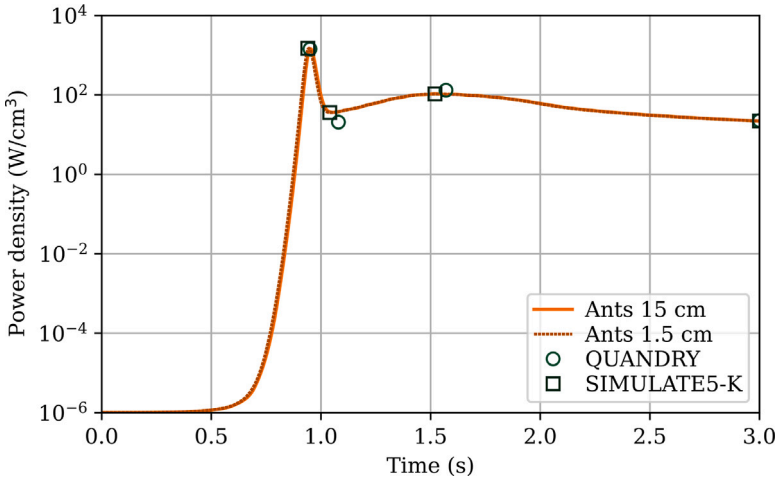

Fig. 7. Time-dependent powers in the LRA single rod benchmark transient. The solution parameters for different programs are presented in Table 9.

Table 8
LRA four rod benchmark transient results.

Code	Ants	Ants	QUANDRY	POLCA-T	SIMULATE5-K
Radial mesh (cm^2)	15 × 15	15 × 15	15 × 15	15 × 15	15 × 15
Axial mesh (cm)	15	1.5	15/30	15/30	15
Number of time steps	820	820	2708	1373	820
Time at first maximum (s)	0.907	0.900	0.914	0.900	0.90
Power at first maximum (W/cm^3)	5797	5606	5532	5754	5626
Time at first minimum (s)	0.996	0.995	1.00	0.993	0.99
Power at first minimum (W/cm^3)	115.9	116.3	128.2	114.5	117
Time at second maximum (s)	1.510	1.510	1.446	1.5	1.49
Power at second maximum (W/cm^3)	368.8	364.2	432.9	368	367
Power at 3.0 s (W/cm^3)	70.9	70.4	72.2	70.6	71
Average fuel temperature at 3.0 s (K)	1010	1010	1018	1011	1016

Table 9
LRA single rod benchmark transient results.

Code	Ants	Ants	QUANDRY	POLCA-T	SIMULATE5-K
Radial mesh (cm^2)	15 × 15	15 × 15	15/30 × 15/30	15 × 15	15 × 15
Axial mesh (cm)	15	1.5	30/37.5	15/30	15
Number of time steps	1200	1200	820	1419	1100
Time at first maximum (s)	0.953	0.946	0.950	0.945	0.94
Power at first maximum (W/cm^3)	1458	1477	1435	1506	1482
Time at first minimum (s)	1.06	1.05	1.08	1.02	1.04
Power at first minimum (W/cm^3)	36.1	35.8	20.7	33.1	36
Time at second maximum (s)	1.52	1.53	1.57	1.52	1.52
Power at second maximum (W/cm^3)	107	105	141	106	106
Power at 3.0 s (W/cm^3)	22.0	21.9	22.6	21.9	22
Average fuel temperature at 3.0 s (K)	499	499	503	–	501

For the four rod transient, the Ants results between a coarse (15 cm node height) and a fine (1.5 cm node height) axial meshes are rather similar. With the finer mesh, the maximum power is obtained slightly earlier and is 3.3 % lower than with the coarser mesh. Overall the behavior of Ants is much closer to POLCA-T and SIMULATE5-K than QUANDRY. The QUANDRY results are calculated with a double node height in the active core region compared with the other programs, but with a denser time stepping. The first minimum power, the second maximum power and the power at 3.0 s are within couple of W/cm^3 between Ants, POLCA-T and SIMULATE5-K. The maximum

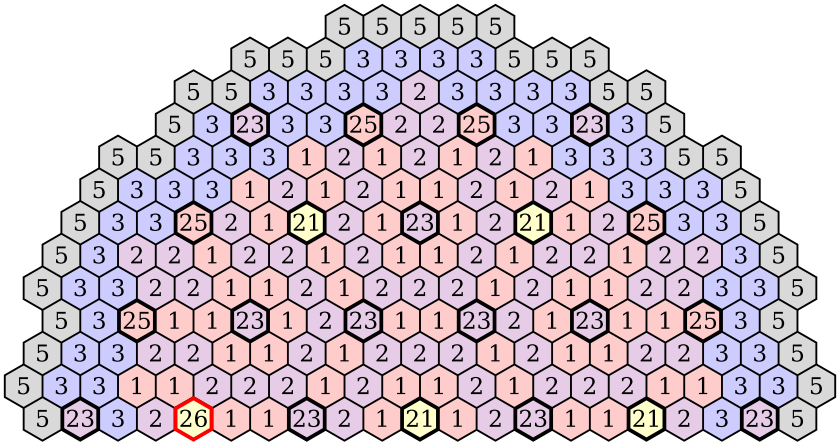

Fig. 8. AER-DYN-001 benchmark half core radial geometry. Bolded assemblies indicate control rod positions. The position of the ejected control rod is outlined with red. Radial reflector positions (material number 5) are absent in the AER-DYN-002 benchmark.

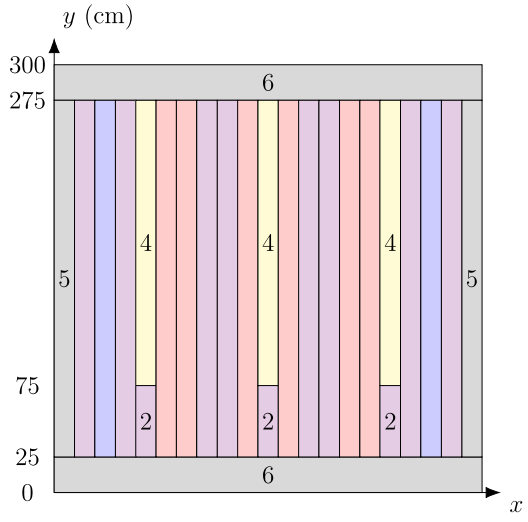

Fig. 9. AER-DYN-001 benchmark axial geometry. Radial and axial reflector regions (material numbers 5 and 6) are absent in the AER-DYN-002 benchmark.

Table 10
LRA benchmark time steps used in the Ants calculations (Smith, 1979; Brega et al., 1981).

Number of time steps			
820		1200	
Time interval (s)	Time step (s)	Time interval (s)	Time step (s)
0.00–0.50	0.012500	0.0–0.2	0.0100
0.50–0.60	0.005000	0.2–0.4	0.0050
0.60–0.70	0.001250	0.4–0.6	0.0020
0.70–0.80	0.000625	0.6–0.7	0.0010
0.80–0.95	0.000500	0.7–1.0	0.0005
0.95–1.00	0.001250	1.0–1.2	0.0025
1.00–2.00	0.010000	1.2–2.0	0.0050
2.00–3.00	0.012500	2.0–3.0	0.0100

power density of the Ants coarse mesh results is closer to the POLCA-T result (0.8 % higher), whereas the fine mesh result is closer to the SIMULATE5-K result (0.4 % lower). All in all, the results between Ants, POLCA-T and SIMULATE5-K are in a rather good agreement, as the maximum power density ranges from 5532 W/cm^3 to 6549 W/cm^3 between various nodal programs using different node meshes and time steppings (Smith, 1979; Brega et al., 1981; Kim and Cho, 2002; Kotchoubey, 2015; Bahadir, 2022).

Also for the single rod transient, the Ants result between the coarse and fine axial meshes are rather similar. With the finer mesh, the maximum power is obtained earlier and is 1.3 % higher than with the coarse mesh. The first minimum and the second maximum powers are 0.9 % and 1.4 % lower for the finer mesh. Overall the behavior of Ants is again much closer to POLCA-T and SIMULATE5-K than QUANDRY. The QUANDRY results are calculated with a much coarser mesh and a sparser time stepping compared with the other programs. The results between Ants, POLCA-T and SIMULATE5-K are in a rather good agreement, as the maximum power density ranges from 1435 W/cm^3 to 1600 W/cm^3 between various nodal programs using different node meshes and time steppings (Smith, 1979; Sutton and Aviles, 1996; Kim and Cho, 2002; Kotchoubey, 2015; Bahadir, 2022).

3.4. AER-DYN-001 benchmark

The AER-DYN-001 benchmark problem (Keresztúri and Telbisz, 2000) describes an asymmetric control rod ejection transient in a three-dimensional VVER-440 core. The benchmark considers only the neutron kinetics without feedback effects. The radial and axial geometry plots of the half of the core are shown in Figs. 8 and 9. The core consists of hexagonal fuel assemblies, and one layer of reflector positions of equal dimensions. The boundary conditions at the outer boundaries of the reflectors are given as extrapolation lengths. The benchmark group constants are given for two energy groups and six delayed neutron precursor groups.

In the initial state of the benchmark, control rod groups 21 and 26 are placed at 50 cm from the bottom of the core, and control rod groups 23 and 25 are fully withdrawn from the core. The transient is initiated by the ejection of control rod 26 at a constant speed in 0.08 s. At 1.0 s after the rod ejection, scram is initiated and the remaining control rod groups are inserted at a constant velocity. The initially withdrawn groups 23 and 25 are inserted from 275 cm to 25 cm from the bottom of the core (top of the bottom axial reflector) in 10 s. The initially partially inserted group 21 is inserted at the same constant velocity from 50 cm to 25 cm from the bottom of the core. The transient is followed for 6 s. In contrast to the benchmark specifications, the moving of the delayed neutron precursors together with the fuel followers when the control rods are inserted is not modeled in Ants. However, the effect of this approximation is likely negligible (Keresztúri and Telbisz, 2000).

The slow insertion of control rods combined with the large node height in this benchmark makes the total power evolution very sensitive to the modeling of partially rodded nodes. Additionally, accurate spatial modeling of the flux is necessary to obtain realistic results for this benchmark. The results obtained with more recent nodal methods (Carreño et al., 2021; Kolev and Christoskov, 2022; Jang et al., 2022)

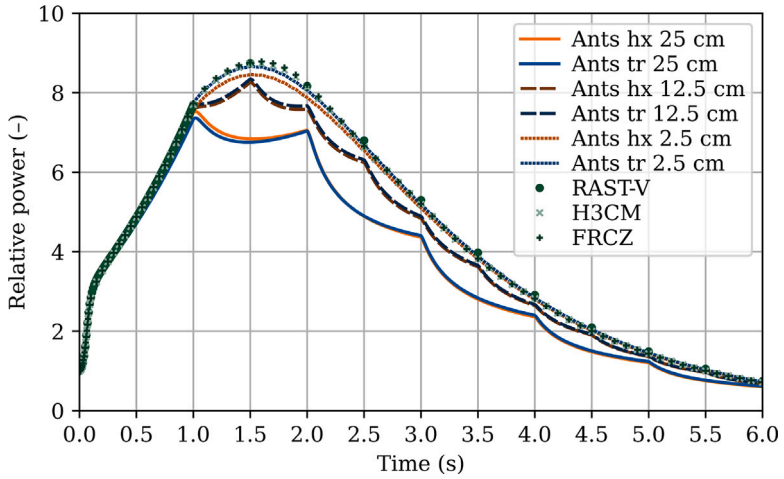

Fig. 10. Time-dependent powers in the AER-DYN-001 benchmark transient. The Ants results are calculated with both hexagonal (hx) and triangular (tr) models.

Table 11
AER-DYN-001 benchmark steady state effective multiplication factors of the initial state and after control rod ejection, and the static reactivity worth $\Delta\rho_{CR} = (1/k_{\text{eff,in}} - 1/k_{\text{eff,out}}) \cdot 100\%$ of the ejected control rod.

Code	Radial mesh (–)	Axial mesh (cm)	$k_{\text{eff,in}}$ (–)	$k_{\text{eff,out}}$ (–)	$\Delta\rho_{CR}$ (%)
Ants	1 hexagon	25.0	0.99942	1.00435	0.4916
Ants	1 hexagon	12.5	0.99941	1.00435	0.4921
Ants	1 hexagon	2.5	0.99940	1.00434	0.4922
Ants	6 triangles	25.0	0.99973	1.00465	0.4900
Ants	6 triangles	12.5	0.99947	1.00442	0.4927
Ants	6 triangles	2.5	0.99939	1.00435	0.4939
RAST-V	6 triangles	12.5	0.99934	1.00432	0.4962
H3CM	1 hexagon	25.0	0.99922	1.00419	0.4956
FRCZ	1536 triangles	25.0	0.99933	–	–

Table 12
Maximum relative powers and their occurrence times in the AER-DYN-001 benchmark.

Code	Radial mesh (–)	Axial mesh (cm)	$t_{\max}$ (s)	$P_{\max}$ (–)
Ants	1 hexagon	25.0	1.02	7.53
Ants	1 hexagon	12.5	1.50	8.26
Ants	1 hexagon	2.5	1.55	8.47
Ants	6 triangles	25.0	1.02	7.36
Ants	6 triangles	12.5	1.50	8.34
Ants	6 triangles	2.5	1.51	8.66
RAST-V	6 triangles	12.5	1.50	8.74
H3CM	1 hexagon	25.0	1.6	8.73
FRCZ	1536 triangles	25.0	1.6	8.73

predict much higher relative maximum powers than those originally published in Keresztúri and Telbisz (2000).

The benchmark results for Ants and a selection of other codes are presented for the initial and after the rod ejection steady state effective multiplication factors, and the static reactivity worth of the ejected control rod in Table 11. The full Ants time-dependent power solutions are presented in Fig. 10 together with comparisons against RAST-V, H3CM and FRCZ. The maximum powers during the transient are shown in Table 12. The data for programs other than Ants is collected from Kolev and Christoskov (2022), Jang et al. (2022), Jang (2022) and Kolev (2022). In comparison to nodal programs Ants, RAST-V and H3CM, FRCZ uses a finite-difference model radially and transverse integration based nodal expansion method (NEM) axially.

The Ants solutions are calculated with a 1 ms time step until 0.2 s and 10 ms afterwards. RAST-V used 10 ms time step until 1.0 s and 500 ms afterwards, whereas H3CM and FRCZ used 5 ms time step until 0.08 s, 10 ms time step until 0.1 s, 50 ms time step until 1.0 s and 100 ms afterwards.

Table 13
Effective multiplication factors of the initial state and after control rod ejection of the AER-DYN-002 benchmark and the static reactivity worth $\Delta\rho_{CR} = (1/k_{\text{eff,in}} - 1/k_{\text{eff,out}}) \cdot 100\%$ of the ejected control rod.

Code	Radial mesh (–)	Axial mesh (cm)	$k_{\text{eff,in}}$ (–)	$k_{\text{eff,out}}$ (–)	$\Delta\rho_{CR}$ (%)
Ants	1 hexagon	25.0	0.99825	1.00869	1.0361
Ants	1 hexagon	12.5	0.99823	1.00868	1.0377
Ants	1 hexagon	2.5	0.99822	1.00867	1.0382
Ants	6 triangles	25.0	0.99854	1.00893	1.0310
Ants	6 triangles	12.5	0.99810	1.00860	1.0433
Ants	6 triangles	2.5	0.99795	1.00850	1.0482
RAST-V	6 triangles	12.5	0.99830	1.00871	1.0338
H3CM	1 hexagon	25.0	0.99800	1.00855	1.0475
FRCZ	384 triangles	25.0	0.99813	–	–
CRONOS	extrapolated	extrapolated	0.99784	1.00846	1.0554

Due to the absence of a proper partially rodded node homogenization method in Ants, the results are presented for the original benchmark nodalization (25 cm node height), a halved node height (12.5 cm) and a fine axial nodalization (2.5 cm node height). RAST-V uses volume weighting of the partially rodded node group constants (Jang, 2022), whereas H3CM and FRCZ use fixed ratios of unrodded and rodded node neutron flux densities obtained from steady state calculations to perform an approximate flux-volume weighting of the group constants (Kolev and Christoskov, 2022).

The k_{eff} values of the Ants hexagonal model are almost constant regardless of the axial mesh used, whereas the triangular model values change when the mesh is refined. It is known from the three-dimensional AER-FCM-001 and AER-FCM-101 steady state benchmarks that the triangular model requires a finer axial mesh to obtain a similar level of accuracy as the hexagonal model (Hirvensalo et al., 2021). However, with a finer mesh, the accuracy surpasses that of the hexagonal model. The RAST-V solutions are calculated using the halved axial node height, whereas H3CM and FRCZ are using the benchmark nodalization. The k_{eff} of RAST-V, H3CM and FRCZ are slightly smaller than those of Ants. The reactivities predicted with RAST-V and H3CM are slightly higher than those calculated with Ants.

From the time-dependent power values, it can be concluded that the coarse mesh results using Ants are obviously erroneous. With the fine axial mesh, the control rod cusping effect is practically indistinguishable. The fine mesh maximum power of the triangular mesh is 2.2 % higher compared with the hexagonal mesh. The presented RAST-V results evading the control rod cusping effect with the relatively large

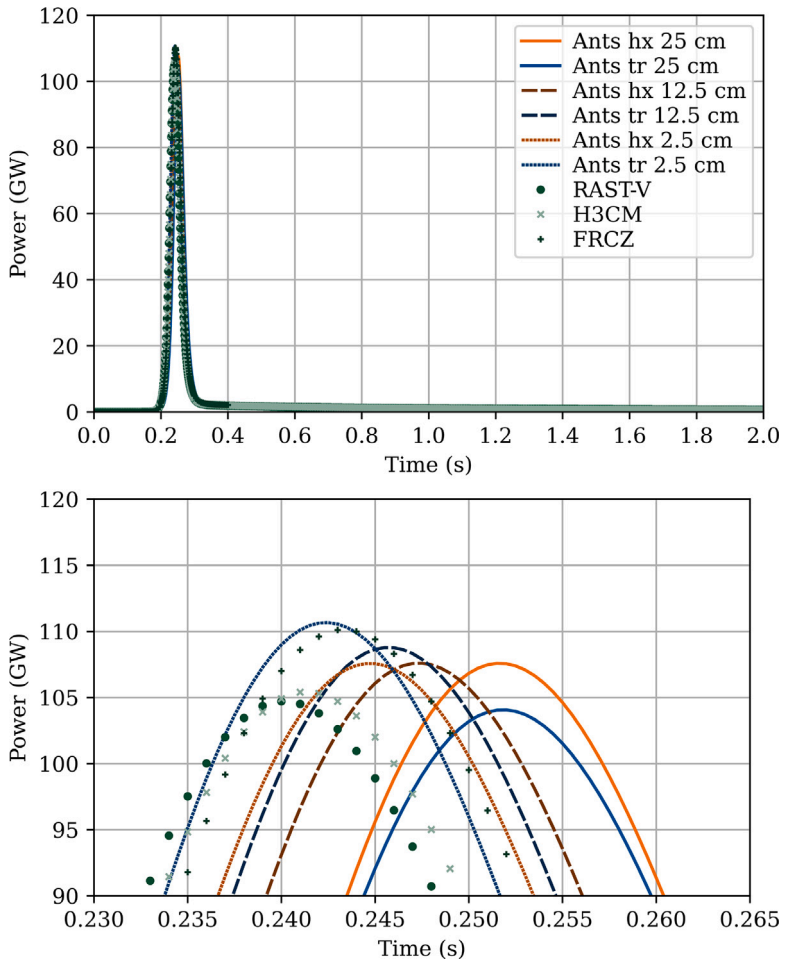

Fig. 11. Time-dependent powers in the AER-DYN-002 benchmark transient (above) with a cropped part showing the maximum powers (below). The Ants results are calculated with both hexagonal (hx) and triangular (tr) models.

time steps are rather well aligned with those of the Ants triangular model and fine axial mesh. The overall behavior of the time-dependent power is very similar between Ants triangular geometry fine mesh calculations and H3CM and FRCZ. Notably, H3CM and FRCZ achieve the maximum power a bit later than Ants. The maximum powers of RAST-V, H3CM and FRCZ are somewhat higher than those of the Ants fine mesh calculations, and are almost equal between the former programs.

3.5. AER-DYN-002 benchmark

The AER-DYN-002 benchmark (Grundmann, 2000) reflects a very similar rod ejection scenario as the AER-DYN-001. However, unlike in the previous problem, no scram is performed and therefore the other control rods remain in their initial positions throughout the transient. Instead, the power increase due to the ejected rod is moderated by a simple Doppler feedback mechanism. The fuel temperature is simulated with a simple adiabatic heating model.

The material parameters and geometry definitions are very similar to the AER-DYN-001 problem. Two energy groups and six delayed neutron precursor groups are used also in this problem, with some minor modifications compared with the AER-DYN-001 problem definitions. The fission cross sections include a feedback term depending on fuel temperature. The radial and axial reflectors are modeled via radial and axial group-dependent albedo boundary conditions. In other words, the reflector nodes shown in the geometry in Figs. 8 and 9 (material numbers 5 and 6) are eliminated completely. Additionally, as scram is not initiated in this problem, the safety control rod groups are not introduced at all.

The transient is initiated by the ejection of rod 26. The rod is ejected at constant speed of 12.5 m/s. The other control rods remain stationary throughout the transient. The transient is followed for 2 s.

Due to the fast ejection of the control rod and the absence of slowly inserted control rods, this benchmark is not susceptible to control rod cusping effects. However, the axial mesh will affect the temperature feedback resolution and possibly the accuracy of the spatial neutronics solution. The reactivity effect of the ejected control rod has been shown to be underestimated in earlier nodal method results compared with fine mesh finite element solutions (Kolev et al., 2001) as highlighted in Makai (2002). Therefore, the results presented in Grundmann (2000) are predicting lower maximum powers in the transient compared with the results obtained with more recent nodal methods (Kolev and Christoskov, 2022; Jang et al., 2022).

The benchmark results for Ants and a selection of other codes are presented for the initial and after the rod ejection steady state effective multiplication factors, and the static reactivity worth of the ejected control rod in Table 13. The full Ants time-dependent power solutions are presented in Fig. 11 together with comparisons against RAST-V, H3CM and FRCZ. The maximum powers during the transient are shown in Table 14. The data for programs other than Ants is collected from Kolev et al. (2001), Kolev and Christoskov (2022), Jang et al. (2022), Jang (2022) and Kolev (2022).

The Ants solutions are calculated with a 0.5 ms time step until 0.5 s and 5 ms afterwards. RAST-V used 1 ms time step for the whole

Table 14
Maximum powers and their occurrence times in the AER-DYN-002 benchmark.

Code	Radial mesh (–)	Axial mesh (cm)	t_{max} (s)	P_{max} (GW)
Ants	1 hexagon	25.0	0.2515	107.6
Ants	1 hexagon	12.5	0.2475	107.6
Ants	1 hexagon	2.5	0.2445	107.6
Ants	6 triangles	25.0	0.2520	104.1
Ants	6 triangles	12.5	0.2455	108.8
Ants	6 triangles	2.5	0.2425	110.7
RAST-V	6 triangles	12.5	0.240	104.7
H3CM	1 hexagon	25.0	0.241	105.4
FRCZ	384 triangles	25.0	0.243	110.1

transient, whereas H3CM and FRCZ used 5 ms time step until 0.2 s, 1 ms time step until 0.3 s and 5 ms afterwards. The FRCZ solution is calculated only up to 0.4 s. The nodalization and partially rodded node group constant homogenization methods are the same as in the AER-DYN-001 benchmark. The temperature feedback of FRCZ is calculated using the coarse mesh nodalization of H3CM. In contrast, the temperature feedback in Ants is calculated separately for each node.

The k_{eff} values of the Ants hexagonal model are practically constant regardless of the axial mesh, whereas for the triangular model they are changing. The triangular model with a finer axial mesh predicts a higher static reactivity worth for the ejected control rod. The RAST-V reactivity is calculated from the exact k_{eff} values shown in Table 13, whereas higher precision values have been used in the calculation of the reactivities of the other programs. Therefore, its exact value might slightly differ from the displayed value. Regardless, it is slightly lower than that predicted with the Ants hexagonal model. The H3CM k_{eff} values are between the two finest axial mesh results of Ants triangular model. The predicted reactivity is therefore also very close to those values, and is higher than the hexagonal geometry results of Ants. The extrapolated finite element method solution with CRONOS predict notably higher control rod worth for the ejected control rod than the rest of the programs.

The maximum powers with the Ants hexagonal model do not depend on the axial mesh. However, with the finer mesh the maximum is obtained slightly earlier. The triangular model maximum power increases when the axial mesh is refined, and the time of the maximum becomes earlier. The RAST-V maximum power is larger than the Ants triangular model coarsest mesh power, but lower than the other results. The Ants results are obtained with halved time step lengths compared with RAST-K. In Ants, using the same 1 ms time step lengths as are used with RAST-K, the maximum powers are approximately 3.8 % smaller than those obtained with the 0.5 ms time step lengths. However, the times of the maximums are unchanged. The 3.8 % smaller value with the same mesh as used by RAST-V coincides rather well with the RAST-V maximum power value. The FRCZ maximum power is rather close to the Ants finest axial mesh triangular geometry result. The H3CM result is lower than most of the Ants results, but slightly higher than the RAST-V result. Overall the behavior of the programs is rather similar, and the differences might be partly explained with the different time steppings used in the calculations.

3.6. Calculation times

Examples of Ants calculation times are presented in this section for the LMW benchmark for the rectangular geometry and the AER-DYN-001 benchmark for the hexagonal and triangular geometries. The cases were selected so that there is no overhead from the simplified thermal hydraulics feedback calculations, although their effect is small. The calculations times here are determined using the same calculation setups as presented in Sections 3.2 and 3.4, including the numbers of axial nodes, number of inner iterations per outer iteration, the convergence criteria and the time step lengths. The calculation parameters, including the number of parallel calculation OpenMP threads and the number of inner iterations per outer iteration, are not optimized for these example cases. Full-core calculations are performed without utilizing any symmetries in the problem geometries. The calculation times include the whole program running times, including the initialization performed by Cerberus. The steady state calculation times are not included in the results. All calculations are performed on similar hardware.

The results for the LMW benchmark using 1 and 10 parallel calculation OpenMP threads are presented in Table 15. With the coarser axial mesh the number of nodes in the calculation model is rather small, and the parallelization does not enhance the performance to a great extent. With the finer axial mesh, a significant advantage is obtained with the greater number of OpenMP threads. With the finer axial mesh, more outer iterations are needed than with the coarser axial mesh model to obtain the desired convergence, thus explaining the more than tenfold calculation times when comparing the single-threaded results.

The results for the AER-DYN-001 benchmark using 1 and 10 parallel calculation OpenMP threads are presented in Table 16. In this benchmark, the number of nodes in the calculation model is great enough also with the coarsest axial mesh for the parallelization to have a visible effect. The magnitude of the calculation time increment when using the triangular model compared with the hexagonal model is in the expected order when taking into account the different number of nodes and analytic basis functions in the models.

3.7. Temporal mesh

The effect of the temporal mesh in the Ants solution is briefly demonstrated using the TWIGL benchmark step perturbation as an example case. The case was selected so that the solutions are not affected by control rod cusping effects or differences in the thermal hydraulics solutions. The benchmark is solved as described in Section 3.1 but with time step lengths 100.000 ms, 50.000 ms, 25.000 ms, 16.667 ms, 12.500 ms, 10.000 ms, 5.000 ms, 2.500 ms, 1.666 ms, 1.250 ms, 1.000 ms, 0.500 ms, 0.250 ms, 0.167 ms, 0.125 ms and 0.100 ms.

The time-dependent powers are compared in Fig. 12 using the finest temporal mesh with the 0.1 ms time step length as the reference. The presented differences are the absolute values of the relative differences at all five common times between the different temporal meshes. In this rather simple benchmark, the relative difference decreases almost linearly at times between 0.2 s and 0.5 s with the time step lengths between 25.000 ms and 0.125 ms. At 0.1 s, the difference decreases even faster as a function of the time step length.

4. Conclusions

A time-dependent solution method of the neutron diffusion equation implemented in the nodal neutron program Ants was described in this paper. Its performance was shown in a series of established two group benchmarks for rectangular, hexagonal and triangular nodal geometries. The solutions produced by Ants agree with the results of other nodal solvers. However, in benchmark problems susceptible to control rod cusping errors, Ants coarse axial mesh results are unsatisfactory due to the lack of a flux-volume weighting routine for the partially rodded nodes. To address this issue, development of a methodology to compute properly homogenized group constants for coarse mesh nodes containing multiple homogeneous materials via solving one-dimensional diffusion equations for axial node stacks, similar to approaches employed in e.g. POLCA-T and SIMULATE5-K (Kotchoubey, 2015; Bahadir, 2022) is underway. In conjunction with the development of the methodology, the moving of the delayed neutron precursors together with the fuel in follower assemblies is planned to be modeled. Currently, the movement is not modeled in Ants. As the benchmarks included in this paper contain either only a simple fuel temperature feedback models or no feedback models at all, the validation process of Ants with coupled neutronics and thermal hydraulics calculations as

Table 15
Ants LMW benchmark absolute and relative calculation times with different axial meshes and number of OpenMP threads. The reference cases in both relative time comparisons are indicated by the relative time 1.00.

Axial mesh (cm)	Time (s)		Relative time 1		Relative time 2	
	Number of threads		Number of threads		Number of threads	
	1	10	1	10	1	10
20	104.1	57.7	1.00	0.55	1.80	1.00
2	1906.5	305.1	18.31	2.93	33.02	5.28

Table 16
Ants AER-DYN-001 benchmark absolute and relative calculation times with different axial and radial meshes and number of OpenMP threads. The reference cases in both relative time comparisons are indicated by the relative time 1.00.

Radial mesh	Axial mesh (cm)	Time (s)		Relative time 1		Relative time 2	
		Number of threads		Number of threads		Number of threads	
		1	10	1	10	1	10
1 hexagon	25.0	3318	528	1.00	0.16	6.28	1.00
1 hexagon	12.5	5963	936	1.80	0.28	11.29	1.77
1 hexagon	2.5	43414	5947	13.09	1.79	82.21	11.26
6 triangles	25.0	12718	2047	3.83	0.62	24.08	3.88
6 triangles	12.5	27190	4152	8.19	1.25	51.49	7.86
6 triangles	2.5	163378	23180	49.24	6.99	309.38	43.89

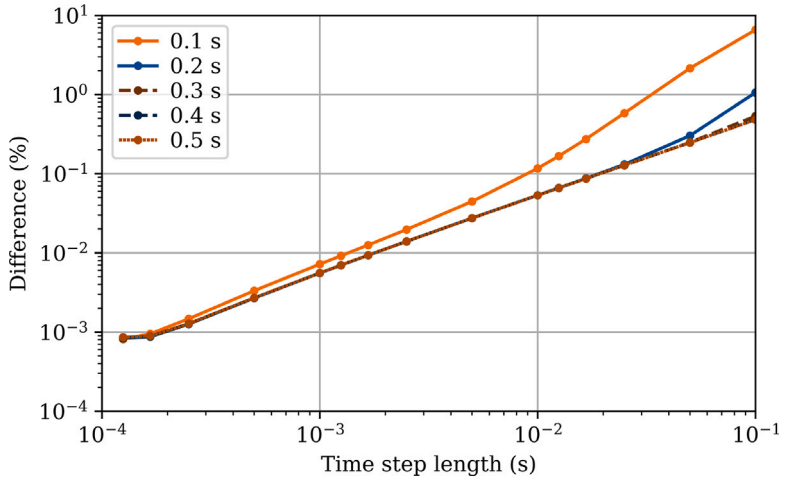

Fig. 12. Absolute values of the relative differences in the time-dependent powers in the TWIGL benchmark step perturbation transient with different time step lengths at the five common times.

a part of the Kraken framework is already being carried on with more detailed benchmarks. Additionally, as all benchmarks in this paper used two energy groups, the evaluation of the Ants time-dependent solution performance for multigroup problems is left for future work.

CRediT authorship contribution statement

Antti Rintala: Conceptualization, Methodology, Software, Formal analysis, Investigation, Writing – original draft, Writing – review & editing, Visualization. **Unna Lauranto:** Methodology, Software, Formal analysis, Investigation, Writing – original draft, Writing – review & editing, Visualization.

Declaration of competing interest

The authors declare that they have no known competing financial interests or personal relationships that could have appeared to influence the work reported in this paper.

Data availability

Data will be made available on request

Acknowledgments

The authors thank Ville Sahlberg for providing a preliminary derivation of the Ants time-dependent neutronics model for the rectangular geometry.

This work has received funding from the LONKERO project under The Finnish Research Programme on Nuclear Power Plant Safety 2019–2022 (SAFIR2022) and the DECAPOD project under The National Nuclear Safety and Waste Management Research Programme 2023–2028 (SAFER2028).

References

Argonne Code Center, 1977. Benchmark Problem Book. Argonne National Laboratory, http://dx.doi.org/10.2172/5037820, ANL-7416 Supplement 2.

Bahadir, T., 2022. Development and benchmarking of transient nodal code SIMULATE5-K neutron kinetics solver. In: Proceedings of the International Conference on Physics of Reactors 2022. PHYSOR 2022, pp. 400–409. http://dx.doi.org/10.13182/PHYSOR22-37639.

Brega, E., Di Pasquantonio, F., Salina, E., 1981. Computation accuracy and efficiency of a coarse-mesh analytic nodal method for LWR transient problems, in comparison with a space-time synthesis method. Ann. Nucl. Energy 8 (10), 509–524. http://dx.doi.org/10.1016/0306-4549(81)90119-5.

Carreño, A., Vidal-Ferràndiz, A., Ginestar, D., Verdu, G., 2021. Adaptive time-step control for modal methods to integrate the neutron diffusion equation. Nucl. Eng. Technol. 53 (2), 399–413. http://dx.doi.org/10.1016/j.net.2020.07.004.

Cho, N.Z., 2005. Fundamentals and recent developments of reactor physics methods. Nucl. Eng. Technol. 37 (1), 25–78.

Cho, N.Z., Kim, Y.H., Park, K.W., 1997. Extension of analytic function expansion nodal method to multigroup problems in hexagonal-z geometry. Nucl. Sci. Eng. 126 (1), 35–47. http://dx.doi.org/10.13182/NSE97-A24455.

Grundmann, U., 2000. AER benchmark specification sheet. URL: https://aerbench.kfki.hu/aerbench/Dyn002.doc. (Accessed 30 September 2022).

Hageman, L., Yasinsky, J., 1969. Comparison of alternating-direction time-differencing methods with other implicit methods for the solution of the neutron group-diffusion equations. Nucl. Sci. Eng. 38 (1), 8–32. http://dx.doi.org/10.13182/NSE38-8.

Hirvensalo, M., Rintala, A., Sahlberg, V., 2021. Triangular geometry model for Ants nodal neutronics solver. In: Proceedings of the International Conference on Mathematics and Computational Methods Applied To Nuclear Science and Engineering, (M&C) 2021. pp. 1859–1868. http://dx.doi.org/10.13182/M&C21-33831.

Jang, J., Personal communication 2022-10-26.

Jang, J., Dzianisau, S., Lee, D., 2022. Development of nodal diffusion code RAST-V for Vodo–Vodyanoi Energeticheskiy reactor analysis. Nucl. Eng. Technol. 52 (9), 3494–3515. http://dx.doi.org/10.1016/j.net.2022.04.007.

Joo, H.G., Park, S.Y., Cho, B.O., Zee, S.Q., 1998. A nonlinear analytic function expansion nodal method for transient calculations. In: Proceedings of the Korean Nuclear Society Spring Meeting. Korean Nuclear Society, pp. 79–86.

Keresztúri, A., Telbisz, M., 2000. AER benchmark specification sheet. URL: https://aerbench.kfki.hu/aerbench/Dyn001.doc. (Accessed 30 September 2022).

Kim, D.S., Cho, N.Z., 2002. Kinetics calculation under space-dependent feedback in analytic function expansion nodal method via solution decomposition and Galerkin scheme. Nucl. Sci. Eng. 140 (3), 267–284. http://dx.doi.org/10.13182/NSE02-A2260.

Kolev, S., Personal communication 2022-11-01.

Kolev, S., Christoskov, I., 2022. A hybrid finite-difference/nodal method for benchmarking the HEXNEM3 coarse-mesh nodal method for time-dependent neutron diffusion applications. Ann. Nucl. Energy 170, 108989. http://dx.doi.org/10.1016/j.anucene.2022.108989.

Kolev, N.P., Lenain, R., Fedon-Magnaud, C., 2001. Finite-element solutions of the AER-2 rod ejection benchmark by CRONOS. In: Proceedings of the Eleventh Symposium of Atomic Energy Research. Kiadja and KFKI Atomenergia Kutatóintézet, Budabest, pp. 395–411.

Kotchoubey, J., 2015. POLCA-T Neutron Kinetics Model Benchmarking (Master Of Science Thesis). KTH Royal Institute of Technology.

Langenbuch, S., Maurer, W., Werner, W., 1977. Coarse-mesh flux-expansion method for the analysis of space-time effects in large light water reactor cores. Nucl. Sci. Eng. 63 (4), 437–456. http://dx.doi.org/10.13182/NSE77-A27061.

Leppänen, J., Valtavirta, V., Rintala, A., Hovi, V., Tuominen, R., Peltonen, J., Hirvensalo, M., Dorval, E., Lauranto, U., Komu, R., 2022. Current status and on-going development of VTT's Kraken core physics computational framework. Energies 15 (3), http://dx.doi.org/10.3390/en15030876, 876.

Makai, M., 2002. AER benchmark site. In: Proceedings of the PHYSOR 2002.

Reed, W.H., Hansen, K., 1970. Alternating direction methods for the reactor kinetics equations. Nucl. Sci. Eng. 41 (3), 431–442. http://dx.doi.org/10.13182/NSE41-431.

Rintala, A., Sahlberg, V., 2019. Extension of nodal diffusion solver of Ants to hexagonal geometry. Kerntechnik 84 (4), 252–261. http://dx.doi.org/10.3139/124.190013.

Sahlberg, V., Rintala, A., 2018. Development and first results of a new rectangular nodal diffusion solver of Ants. In: Proceedings of the PHYSOR 2018. pp. 3861–3871.

Smith, K.S., 1979. An Analytic Nodal Method for Solving the Two-Group, Multi-dimensional, Static and Transient Neutron Diffusion Equations (Master's thesis). Massachusetts Institute of Technology.

Sutton, T., Aviles, B., 1996. Diffusion theory methods for spatial kinetics calculations. Prog. Nucl. Energy 30 (2), 119–182. http://dx.doi.org/10.1016/0149-1970(95)00082-U.

Tuominen, R., Valtavirta, V., 2023. BEAVRS pin-by-pin calculations with Ants-SUBCHANFLOW-SuperFINIX code system. Ann. Nucl. Energy 180, http://dx.doi.org/10.1016/j.anucene.2022.109447, 109447.

Valtavirta, V., Rintala, A., Lauranto, U., 2022a. Pin power reconstruction for hexagonal geometry in nodal neutronics program Ants. Ann. Nucl. Energy 179, http://dx.doi.org/10.1016/j.anucene.2022.109384, 109384.

Valtavirta, V., Rintala, A., Lauranto, U., 2022b. Validating the Serpent-Ants calculation chain using BEAVRS fresh core hot zero power data. J. Nucl. Eng. Radiat. Sci. 8 (4), http://dx.doi.org/10.1115/1.4052731, 044504.

Valtavirta, V., Tuominen, R., 2021. A simple reactor core simulator based on VTT's Kraken computational framework. In: Proceedings of the International Conference on Mathematics and Computational Methods Applied To Nuclear Science and Engineering, (M&C) 2021. pp. 304–313. http://dx.doi.org/10.13182/M&C21-33704.

Woo, S.W., Cho, N.Z., Noh, J.M., 2001. The analytic function expansion nodal method refined with transverse gradient basis functions and interface flux moments. Nucl. Sci. Eng. 139 (2), 156–173. http://dx.doi.org/10.13182/NSE01-A2229.

Xia, B., Xie, Z., 2006. Flux expansion nodal method for solving multigroup neutron diffusion equations in hexagonal-z geometry. Ann. Nucl. Energy 33 (4), 370–376. http://dx.doi.org/10.1016/j.anucene.2005.06.011.

Xia, B., Xie, Z., Xian, C., Yao, D., 2006. Flux expansion nodal method for solving static and transient neutron diffusion equations in hexagonal-z geometry. In: Proceedings of PHYSOR-2006.